IEEE Photonics Journal
An IEEE Photonics Society Publication

Open Access

# Optical Beam Induced Current and Time Resolved Electro-Luminescence in Vertical Cavity Surface Emitting Lasers During Accelerated Aging

Volume 11, Number 5, October 2019

Adam W. Bushmaker
Zachary Lingley
Miles Brodie
Brendan Foran
Yongkun Sin

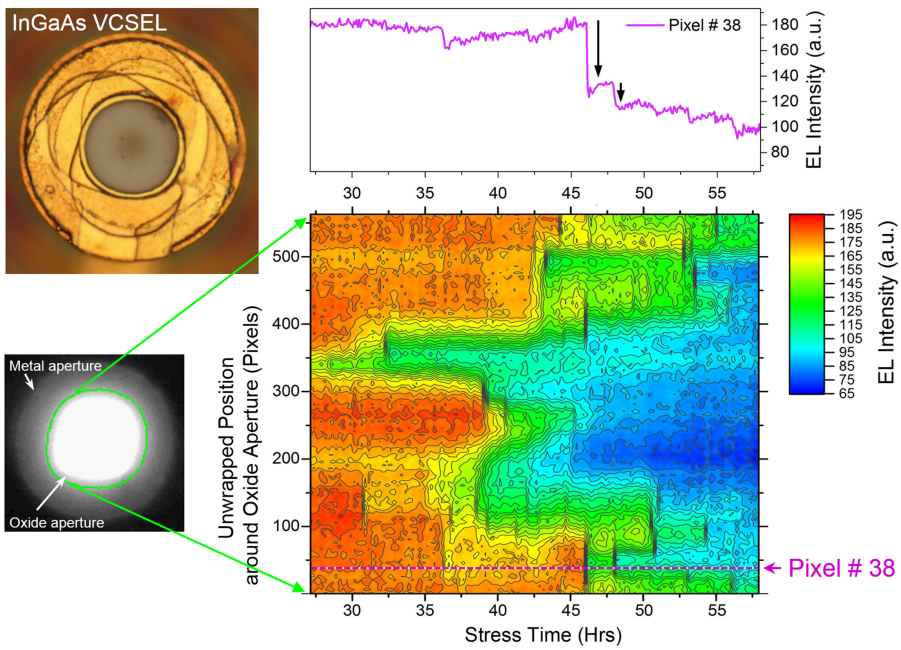


DOI: 10.1109/JPHOT.2019.2934945

# Optical Beam Induced Current and Time Resolved Electro-Luminescence in Vertical Cavity Surface Emitting Lasers During Accelerated Aging

**Adam W. Bushmaker, Zachary Lingley, Miles Brodie, Brendan Foran, and Yongkun Sin**

Department of Microelectronics Technology, The Aerospace Corporation, El Segundo, CA 90245 USA

*DOI:10.1109/JPHOT.2019.2934945*


Manuscript received July 29, 2019; accepted August 7, 2019. Date of publication August 12, 2019; date of current version August 29, 2019. This work was supported by the Independent Research and Development program at The Aerospace Corporation. Corresponding author: Adam W. Bushmaker (e-mail: adam.bushmaker@aero.org).

**Abstract:** Vertical Cavity Surface Emitting Lasers are characterized under a high magnification optical microscope for reliability during accelerated aging using Optical Beam Induced Current and Electroluminescence imaging and spectroscopy, and also with electrical IV characterization. EL image data is captured with time resolution during device failure, and compared to the OBIC images, yielding insight into failure mechanisms. In particular, sudden, localized, permanent reductions in EL intensity around the outside of the laser oxide aperture are observed during the period of failure, indicating step-wise rather than gradual degradation in laser performance. These failure events are temporally correlated with sudden increases in low-injection junction current. Both OBIC and IV characterization suggest mid-gap defect formation as the cause of the observed failures.

**Index Terms:** Vertical cavity surface emitting lasers, optical beam induced current, electroluminescence.

## 1. Introduction

Vertical Cavity Surface Emitting Lasers (VCSELs) have been adopted rapidly in many fields, including remote sensing, illumination, laser excitation, and short-haul high data-rate fiber communications. This is due to a number of advantageous attributes offered by VCSEL technology, such as low cost, small size, high speed, and a native circular beam shape [1]–[4]. The low cost of manufacture has driven their adoption in some applications, such as computer laser mice, and resulted in high volume production, with one manufacturer (Philips) having shipped its billionth VCSEL device in late 2018. One of the most promising applications for VCSEL technology is high data-rate fiber communications, where VCSELs can send digital data at rates up to 56 Gb/s over short distances [5]. This has found applications in a variety of industries, from server centers to avionics.

VCSEL reliability has been investigated by many research groups, notably Herrick *et al.* [6]–[9]. Due to the complicated structure of these devices, VCSELs must be designed with electrical, mechanical, optical, and thermal considerations taken into account. There are many possible failure modes in VCSELs, including semiconductor lattice defects such as the so-called “Dark-line” defects, dopant migration, non-uniform current injection, and copper poisoning [9].

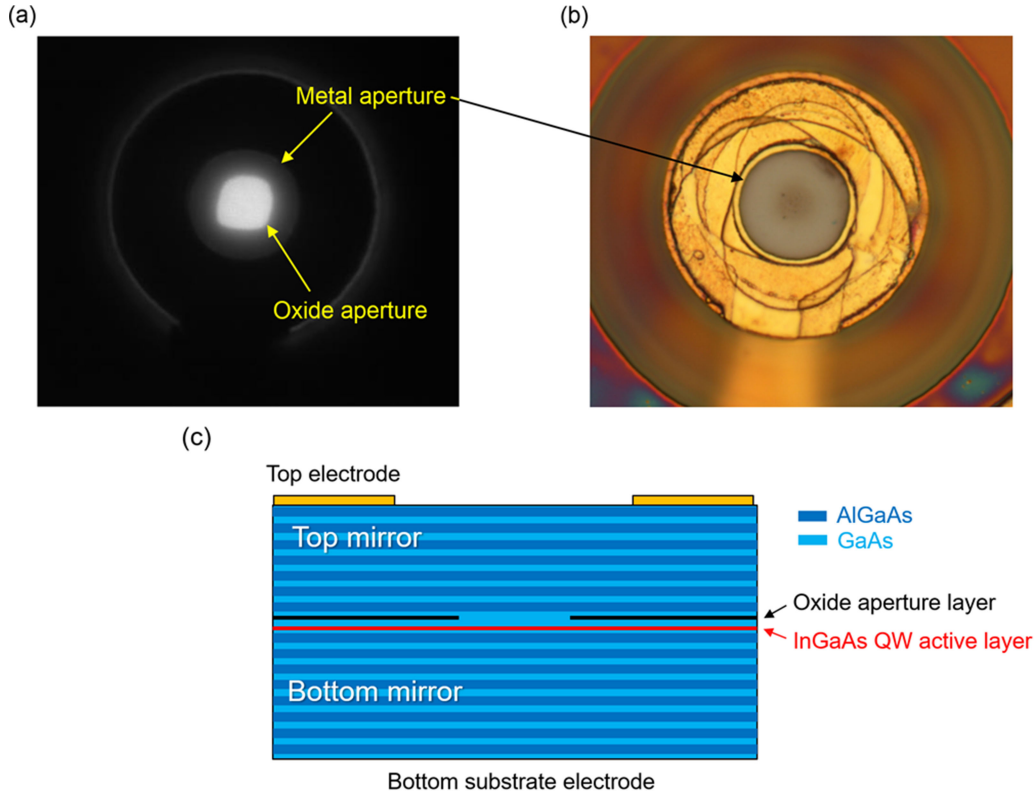


Fig. 1. (a) Electroluminescence micrograph focused on the VCSEL active layer during operation with a junction current of 1.65 mA, (b) reflectance micrograph focused on VCSEL top surface, and (c) device cross-sectional diagram, showing the top electrode (which forms the metal aperture), the oxide aperture, the QW active layer, and the Distributed Bragg Reflector (DBR) mirrors.

One powerful technique for investigating VCSEL failures and reliability is electroluminescence (EL) imaging, in which light emitted by the device is imaged under a microscope. EL imaging is useful because it directly measures the electro-optical conversion efficiency of the device with spatial resolution, allowing for localization of performance limiting defects. For instance, crystallographic defects known as “dark-line defects” can be identified and localized [7], and this information can be used for targeted destructive physical analysis (DPA) using Focused Ion Beam (FIB) cross-sectioning and subsequent Scanning Electron Microscope (SEM) and Transmission Electron Microscope (TEM) imaging.

While these previous studies have identified and characterized different failure mechanisms using static EL imaging before and after failure, only one study has been published showing time resolved EL imaging in VCSELs [6], with EL image data at three different stress times.

In this study, EL image data from commercial 980 nm VCSELs were collected with fine temporal resolution during accelerated aging of the device under both thermal and electrical stress. The resulting data allows for insights into failure growth patterns and spatial information not possible with static imaging of completely failed devices, and show a step-like failure at discrete locations around the oxide aperture perimeter. Optical microscope images of these devices are shown in Fig. 1(a) (EL image) and Fig. 1(b) (reflectance image). The EL images were collected using the same microscope as the reflectance image, by turning off the microscope illuminator and adjusting the camera integration time to a duration appropriate for the EL emission.

A SEM image of one of the devices tested is shown in Fig. 2(a), and cross sectional TEM images of one of the devices is shown in Figs. 2(b) and 2(c). By imaging the active layer of the device with time-resolution during accelerated aging, we could perceive the development of defects that

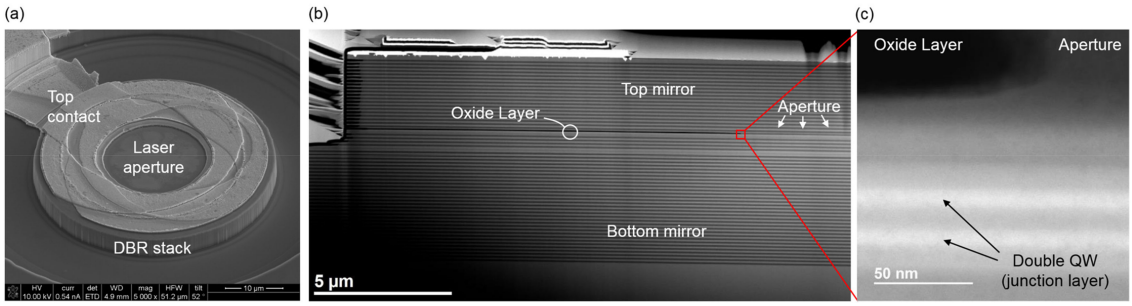


Fig. 2. (a) SEM image of VCSEL device showing device structures, (b) Cross sectional TEM image of VCSEL device, and (c) high resolution TEM image of the active layer at the edge of the oxide aperture. Various device structures can be seen, including the top and bottom DBR mirrors, oxide aperture, and the double quantum well active layer. Fig. 2(b) shows only one-half of the VCSEL cross section, with the center axis of the VCSEL corresponding approximately to the right edge of the image.

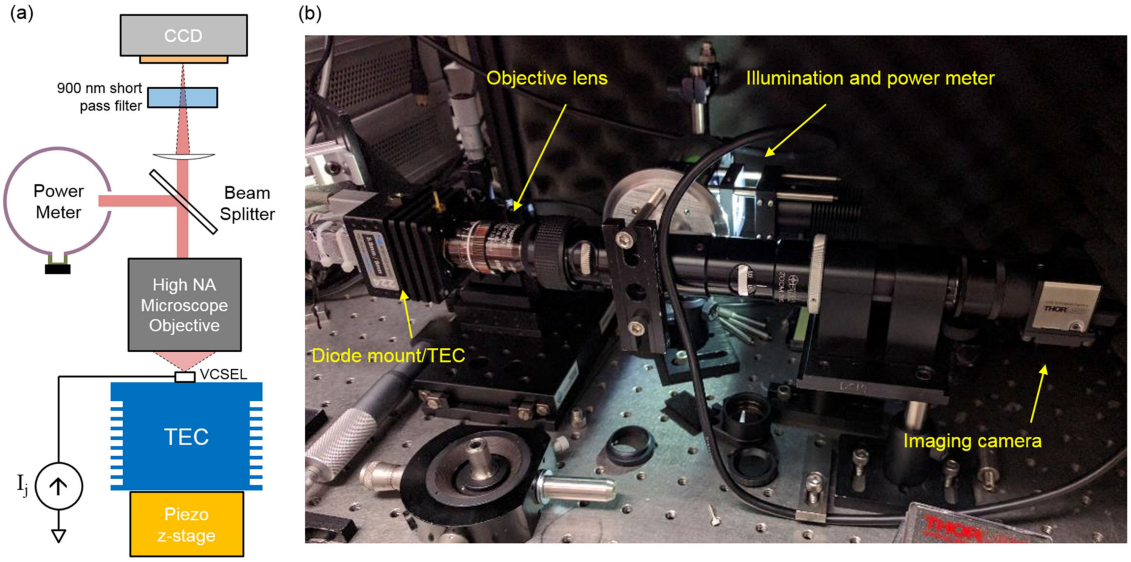


Fig. 3. (a) Diagram and (b) photograph of the time-resolved VCSEL accelerated ageing EL imaging test setup.

ultimately lead to the device failure. In addition to this time-resolved measurement, devices were also characterized before and after failure with EL spectroscopy and optical beam induced current (OBIC) imaging and spectroscopy. These techniques are similar to our previous work on edge emitting high power laser diodes (EE-HPLDs) [10].

## 2. Experimental Details

### *2.1 Time Resolved Electroluminescence Imaging*

Time resolved EL measurements were performed on a custom-built microscope with a thermoelectric cooler (TEC) temperature controlled diode mount, as shown in Fig. 3. The EL emission was imaged through a 900 nm short-pass filter, to filter out the 980 nm laser light and only allow higher energy photons emitted through spontaneous emission to reach the camera. A Thorlabs DCC3240N USB CMOS camera was used to capture EL emission images. The sample was illuminated with light from a LED, coupled to the sample through a partially reflective mirror in the microscope body and an external beamsplitter. During electrical stress, the emitted laser light was coupled to

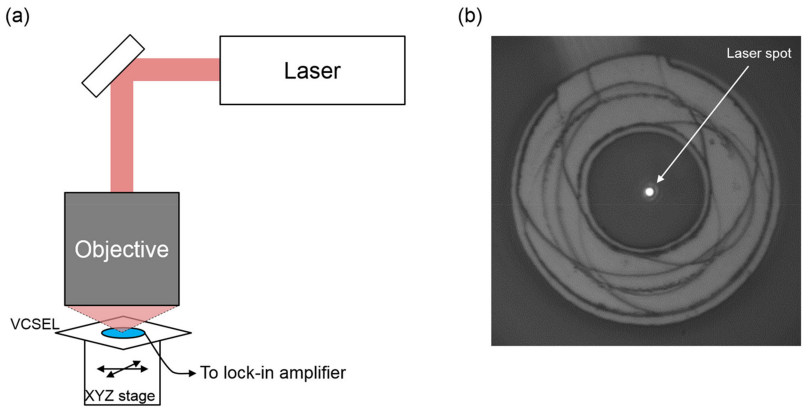


Fig. 4. (a) Optical Beam Induced Current (OBIC) experimental setup, (b) reflectance micrograph image showing the laser spot focused onto the VCSEL aperture.

an ILX Lightwave OMM-6810B optical power meter with a Silicon detector head and integrating sphere through the same partially reflective mirror and external beam-splitter. In order to measure and factor out the laser light power losses through the optical components in the microscope, the measured VCSEL power through the complete microscope was compared to measurements made with same VCSEL coupled directly into the integrating sphere of the power meter.

### 2.2 Long-Term Imaging Stability

Thermal and mechanical X-Y drift of the sample/microscope (within the focal plane) during the test was corrected for in post-processing by shifting the images so that the VCSEL aperture remains in the same place throughout the test. This was done using the LabVIEW image processing package. Thermal and mechanical drift in the Z direction (out of the focal plane) caused the VCSEL aperture to de-focus, blurring the images, and so post-processing image shift as in the X-Y correction was not an option. Drift in the Z-direction was corrected for with a piezo-controlled actuator (shown in Fig. 3(a)) and a contrast-based auto-focus algorithm which calculated the optimum focal plane distance from reflectance images captured by the microscope camera in real-time. During the entire accelerated aging test, no changes were observed in the VCSEL reflectance images, and this method was found to reliably track and correct for the focal plane drift throughout the course of the experiment. These corrections were essential for this test, due to the large thermal gradients caused by the elevated sample temperature and long time periods involved.

Between periods of electrical stress, EL emission from the device active layer was driven by a small current (1.65 mA) and imaged with the microscope camera.

### 2.3 Optical Beam Induced Current Imaging

In addition to EL imaging, devices were characterized with OBIC imaging. Excitation light from a NKT SuperK Extreme supercontinuum laser, monochromated using an acousto-optic tunable filter, was focused on the VCSEL active layer using a high numerical aperture objective lens, as shown in Fig. 4(a). An optical microscope image of the VCSEL with the laser spot focused to a diffraction limited spot is shown in Fig. 4(b). The selected excitation wavelength could be varied over a wide range from 550 nm to 1400 nm using the tunable filter. The excitation light was modulated at 10 kHz, and the resulting electrical signal generated in the VCSEL was measured using the current preamplifier input of a SR830 lock-in amplifier.

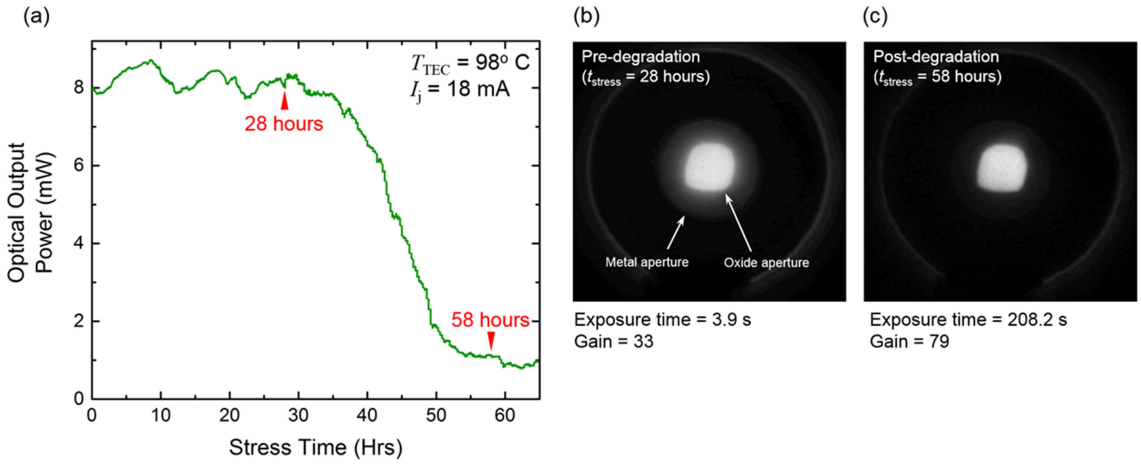


Fig. 5. Optical laser power output at 980 nm plotted versus stress time (a), with the TEC mount temperature set to 98° C, and a current of 18 mA for both stress and optical output power measurement. The device optical power output starts to permanently degrade at ~35 hours stress time. Low current (1.65 mA) EL emission images were captured with a 900 nm low pass filter, taken at 28 hours (b) and 58 hours (c) stress time. Throughout the experiment, camera integration time and gain were increased to maintain a constant maximum EL pixel intensity, despite decreasing EL efficiency.

## 3. Results

The VCSEL power output at 980 nm for one of the devices tested is plotted versus stress time in Fig. 5(a). Power output held at approximately 8 mW for the first 35 hours of stress, after which power began to decrease until reaching 1 mW at approximately 55 hours stress time, after which the power output plateaued. Figs. 5(b) and 5(c) show images of the EL emission at low bias current captured before (b) and after (c) VCSEL power output degradation, as viewed through a 900 nm shortpass filter. The images show bright EL emission in the center of the oxide aperture, and weaker EL emission between the oxide aperture edge and metal aperture edge. During the test, an automatic gain and exposure control (AGC) algorithm was used to keep the maximum pixel intensity constant as the VCSEL degraded. Low-bias EL intensity, as determined from the exposure time and gain of the EL images, was nearly constant through the beginning of the experiment up until 28 hours stress time. After this, the low-bias EL intensity dropped by approximately two orders of magnitude during failure, as can be seen by noting the increase in gain and exposure time required to obtain the same EL image intensity at 58 hours stress time. This is a much larger change in intensity than that measured for the high-current laser light power emission, which only decreases by a factor of 8x during the same time period (Fig. 5(a)). Spectral measurements of the EL emission from post-failure VCSELs showed an increased proportion of the EL laser light at 980 nm, with decreasing proportion of spontaneous emission at shorter wavelengths. This spectral shift could explain some of the observed decrease in EL emission intensity, because of the 900 nm short pass filter used during these measurements.

Since the maximum EL emission intensity in our devices occurred in the middle of the oxide aperture, the AGC algorithm results in a nearly constant pixel intensity in this location throughout the test. In contrast, the measured EL pixel intensity outside the oxide aperture decreased during stress, despite the increased integration time and camera gain. As a result, after failure, a smaller percentage of the total EL emission came from outside of the oxide aperture, as can be seen when comparing Figs. 5(b) and 5(c).

Plotted in Fig. 6 are the spatial and temporal EL imaging results during accelerated stress. Fig. 6(a) shows a representative EL image, with bright EL emission in the center of the oxide aperture, and weaker EL emission between the oxide aperture edge and the metal aperture edge. The EL intensity around the outside of oxide aperture was measured along a profile denoted by the green line in Fig. 6(a), and is unwrapped and plotted in Fig. 6(c) as a function of time. In this contour

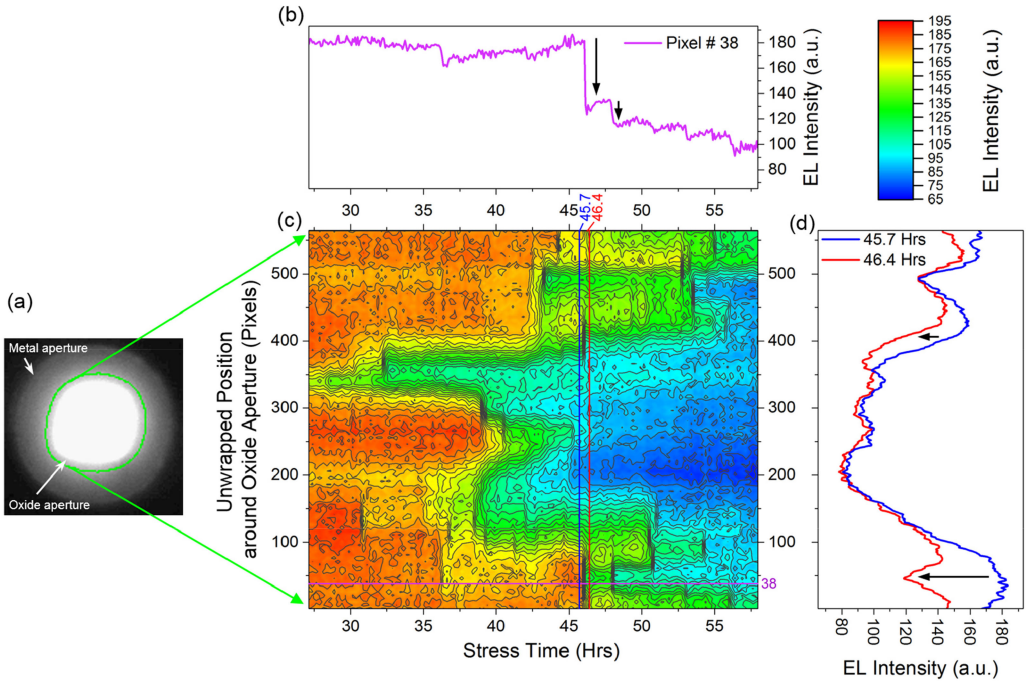


Fig. 6. Low-current bias EL intensity around the outside of the oxide aperture plotted versus time. (a) oxide aperture with intensity cross section denoted by green line around aperture, (b) EL intensity at pixel #38 versus stress time, (c) contour plot showing EL intensity versus time and pixel position, and (d) EL intensity versus pixel position before (blue) and after (red) a localized failure event characterized by a decrease in EL intensity.

plot, discrete, localized failure events can be seen around outside of the oxide aperture, where the EL intensity suddenly drops by up to ~30%. These large drops occur over small spatial regions corresponding to only 10%–15% of the total oxide aperture perimeter. Several of these EL intensity drops are highlighted in Figs. 6(b) and 6(d), which show the intensity versus time and position, respectively, for selected locations and times, respectively. Approximately 20 discrete failure events can be seen in the data. No such events were observed in the time leading up to failure.

In addition to EL images, device junction IV curves were also measured periodically using an Agilent Semiconductor Parameter Analyzer (Model 4155C) at room temperature during the stress, as shown in Fig. 7(a). Very different IV characteristics were obtained after the device failed, with the low-bias current levels increasing by over two orders of magnitude during the period of failure. The quality of a laser diode active layer can be studied by comparing the forward current measured from the device because the bulk recombination current term or $2kT$ term of the forward current includes a trap density in its prefactor. The bulk recombination current density is given by the following expression [11]:

$$J_F \cong \frac{qW}{2} \cdot \sigma \cdot v_{th} \cdot N_t \cdot n_i \cdot \exp\left(\frac{qV}{2kT}\right) \tag{1}$$

where $q$ is the electronic charge, $W$ is the depletion region width, $\sigma$ is the capture cross section, $v_{th}$ is the thermal velocity, $N_t$ is the trap density, $n_i$ is the intrinsic carrier concentration, $k$ is Boltzmann's constant, and $T$ is the absolute temperature. The following assumptions are made in comparing trap densities of the device before and after the failure: (1) The increase in current with stress is a result of trap-assisted recombination according to the Shockley-Read-Hall (SRH) model with a single energy level trap, (2) we only consider Eq. (1) as an approximation for the low-level injection generation-recombination current region, (3) bulk recombination current dominates surface recombination current, (4) The product of $\sigma$ and $v_{th}$ remains the same throughout device

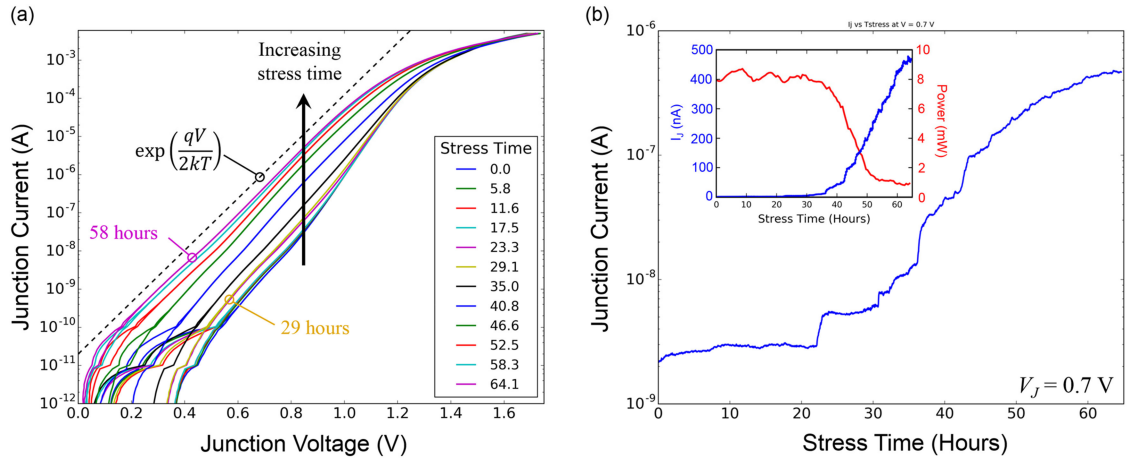


Fig. 7. VCSEL electrical characteristics versus stress time. (a) Forward-bias IV curves from the device shown in Fig. 6, measured periodically over time during stress, and (b) junction current measured at 0.7 V (from (a)) plotted versus stress time. The inset shows the same junction current data plotted on a linear y-axis along with the laser power output during stress (junction current = 18 mA). During device failure, the low bias junction current increased by over two orders of magnitude. The dashed line in (a) indicates the *qV/2kT* slope, corresponding to the generation-recombination regime.

failure. Assumption (1) is validated by the fact that the ideality factor (*n*) of the IV curves during and after failure is approximately 2, correspond to the *2kT* term, which is illustrated in Fig. 7(a) by the dashed line. Fig. 7(b) shows the junction current at a forward bias of 0.7 V plotted versus stress time. The pristine device had a junction current of ∼2 nA, which rose to ∼500 nA after stress. Thus, Eq. (1) predicts an increase in trap density of ∼250x for the device after failure. The degradation started around 22 hours, and the bulk of the degradation occurred after 30 hours stress time, corresponding to the period of observed failure as measured by high-bias laser power output and EL imaging. After ∼40 hours stress time, the low-level junction current increased linearly, as can be seen in the inset of Fig. 7(b). Also plotted in the inset of Fig. 7(b) is the VCSEL high-bias optical power output plotted versus stress time for comparison. Low-level junction current increased for some time (as seen in the log plot) before laser power output power starts to decrease, indicating that there is some minimum defect density that must be exceeded before laser operation is affected.

The low-injection junction current increased non-linearly, with sudden jumps that were temporally correlated with the discrete failure events observed in the EL data. This is illustrated in Fig. 8, which re-plots the EL intensity versus stress time data Fig. 8(a), along with the relative change in junction current, given by the derivative of the junction current $dI_J/dt$ divided by the junction current $I_J$ itself. After approximately 47 hours stress time, the failure events in the electrical data are weaker in intensity, possibly due to the higher overall junction current. The temporal correlation of the optical and electrical signatures indicates a common cause for the observed failure events.

OBIC images of different devices under test were captured using a raster-scanned piezo-driven XY-stage over an area of 20 $\mu$m × 20 $\mu$m. Images generated using this technique are shown below, with images for both pristine (Figs. 9(a) and 10(a)) and failed (Figs. 9(b) and 10(b)) devices. OBIC images were not captured with time resolution during failure, like the EL images. Fig. 8 shows OBIC images for excitation at 880 nm, where carriers were promoted across the band gap of the InGaAs quantum wells. Excitation of pristine devices at this wavelength generated strong OBIC within the oxide aperture, and weaker OBIC outside the oxide aperture, as shown in Fig. 9(a). In devices that had been failed through accelerated ageing, the OBIC outside the oxide aperture was strongly suppressed relative to pristine levels, as shown in Fig. 9(b). Fig. 10 shows OBIC images for excitation at 1100 nm. At this wavelength, the photon energy is less than the band gap of the InGaAs quantum wells. As shown in 10(a), pristine devices showed negligible OBIC signal generation at this excitation wavelength. However, in failed devices, OBIC generation was observed around the

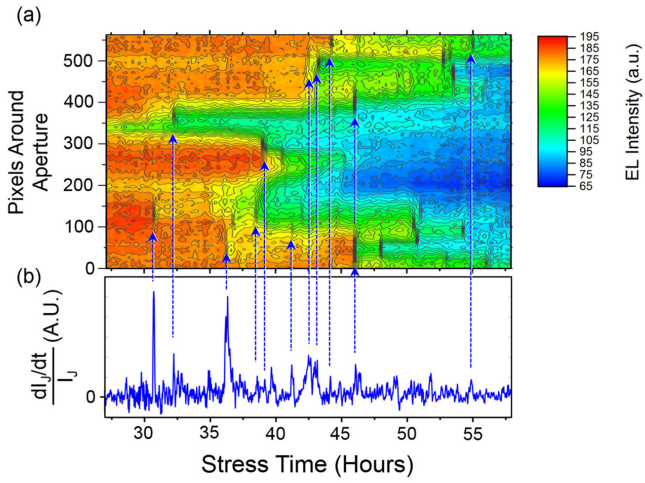


Fig. 8. Temporally correlated optical and electrical failure event signatures. (a) EL emission intensity plotted versus position around aperture circumference (y-axis) and stress time (x-axis), and (b) relative change in junction current plotted versus stress time. EL intensity data plotted in (a) is the same as data plotted in Fig. 6(c). Data plotted in (b) was calculated from junction current data plotted in Fig. 7(b), which was measured at a constant junction voltage of 0.7 V.

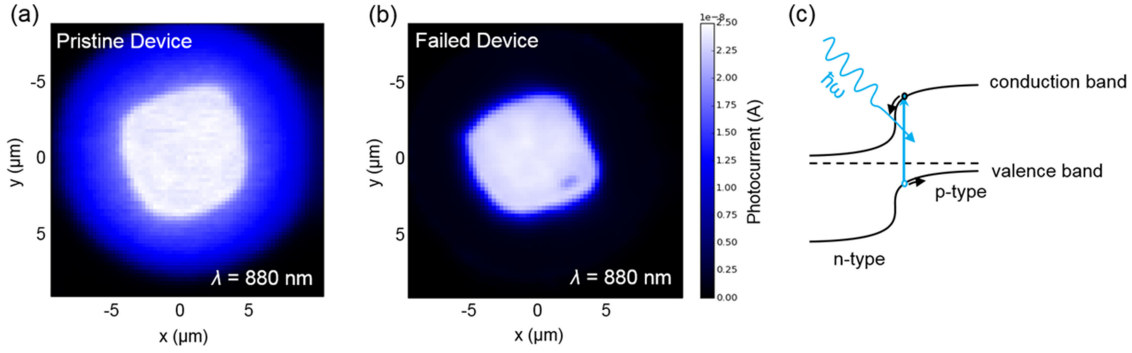


Fig. 9. Optical Beam Induced Current (OBIC) images of (a) a pristine device, and (b) a failed device, with laser excitation wavelength 880 nm, which is above the band gap energy of the active layer, resulting in photocurrent generation as illustrated in (c), notional band diagram of VCSEL diode junction showing the photon absorption and current generation in the OBIC process. The failed device shows weaker photo current generation than the pristine device outside the oxide aperture. Images in (a) and (b) were taken from different devices with the same laser power (~3 $\mu$W) and photocurrent gain settings, and have the same z-scale.

edge of the oxide aperture, as shown in Fig. 10(b). This ring of OBIC signal shows spatial structure, indicating localized regions of light absorption. Both 880 nm images in Fig. 9 were taken with the same laser power (~3 $\mu$W) and photocurrent gain settings, and both 1100 nm images in Fig. 10 were taken with the same laser power (~80 $\mu$W) and photocurrent gain settings (different from those in Fig. 9). Images shown in Figs. 9(a) and 10(a) are from the same pristine device, and images shown in Figs. 9(b) and 10(b) are from the same failed device.

## 4. Discussion

The band of 1100 nm OBIC signal around the oxide aperture edge in the failed VCSEL shown in Fig. 10(b) likely correspond to mid-gap defect states, as shown in the cartoon band diagram drawn in Fig. 10(c). These mid-gap defect states are created at failure sites possibly due to crystallographic defects in the material. Furthermore, the localized nature of these defect sites in Fig. 10(b) indicates

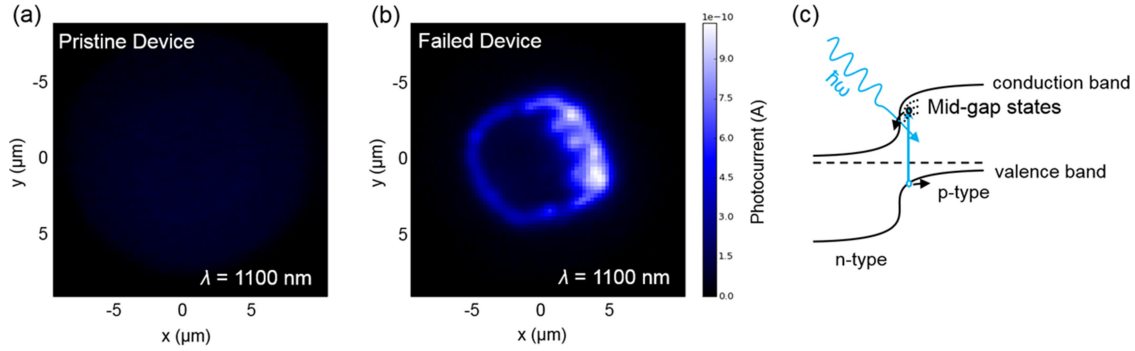


Fig. 10. Optical Beam Induced Current (OBIC) images of (a) a pristine device, and (b) a failed device, with laser excitation wavelength 1100 nm, which is below the band gap energy of the active layer, resulting in photocurrent generation from mid-gap states as shown in (c). The pristine device shows negligible photocurrent generation, while the failed device shows localized photocurrent generation at the oxide aperture edge. Images in (a) and (b) were taken with the same laser power (∼80 $\mu$W) and photocurrent gain settings, and have the same z-scale. Images from Fig. 9(a) and Fig. 10(a) are from the same device, and images from Fig. 9(b) and 10(b) are from the same device.

discrete failure sites, rather than uniformly failed material. The signal observed during excitation with sub-bandgap laser energy has frequently been referred to in the literature as Thermal Induced Voltage Alteration (TIVA) [12]. However, it may not be appropriate in this case, since an external bias is needed to observe TIVA signals, which are usually attributed to thermally induced changes in conductance. These conductance changes are measured through voltage fluctuations created by passing a small externally applied bias current through the device under test [13], [14]. In this measurement, no externally applied bias was used, and signals are observed using a current preamplifier, rather than a voltage amplifier. It is possible that the observed signals come from Seebeck Effect Imaging (SEI) [13], [14], which are generated by temperature gradients in areas exhibiting the Seebeck effects, as in a thermocouple or thermoelectric semiconductor junction. In SEI, signal generation is possible in the absence of any applied bias voltage or current. However, one hallmark of SEI signals is a bi-polar signal from different areas of the device, due to the possibility for positive and negative thermal gradients. No bi-polar signals were observed in this study. This may simply be due to the fact that the Seebeck effect is being generated by the different thermoelectric coefficients in the p-/n-type layers above/below (respectively) the active layer. This fixes the polarity of possible SEI signals originating from the junction layer, where all the defects are located. Practically, it may be difficult to tell the difference between sub-bandgap defect state OBIC and SEI signals, as they are both generated by light absorption at sub-bandgap defect sites, and both result in current measured through the junction.

The observation of increased generation-recombination current during stress corresponding to the *2kT* term in the SRH equation provides further evidence for the creation of mid-gap defect trap states. The temporal correlation of the optical and electrical signals indicates that the failure events observed with EL measurements have a common cause as those observed in the low-bias junction current, and that this common cause involves the formation mid-gap trap states at defect sites.

The observed EL emission outside the oxide aperture is interpreted as leakage current in the p-type material above the active layer. This leakage current is comprised of holes which pass around the edge of the oxide aperture and are then transported horizontally outward away from the center axis of the VCSEL through a gap between the oxide and active layers, as shown in Fig. 11. A similar leakage transport process occurs in reverse during OBIC imaging, when the laser spot is outside the oxide aperture, generating electron-hole pairs in this region.

The hypothesis of discrete failure sites is further supported by the data shown in Fig. 6, which shows sudden, drastic decreases in EL intensity, which occurred at different times at different locations around the oxide aperture. It is likely that the failure sites which exhibit mid-gap states observed in Fig. 10(b) also reduce hole transport in this region. This could be due to carrier

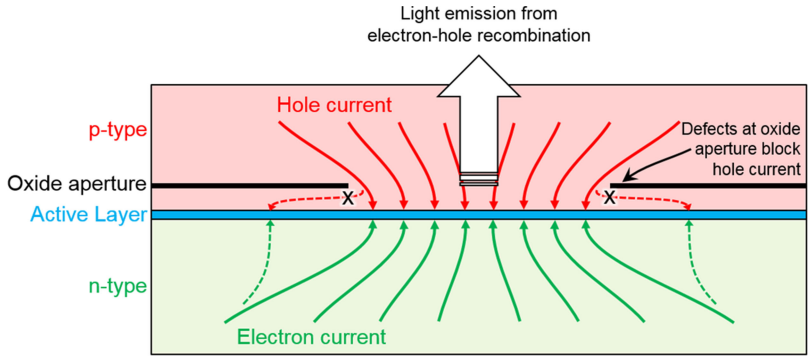


Fig. 11. Cartoon diagram illustrating hole leakage current as the source of light emission outside the edge of the oxide aperture in pristine VCSELs. Defects at the oxide aperture edge are proposed as a barrier to this leakage current, resulting in reduced OBIC and EL signals.

scattering and reduced mobility at the defect sites, and/or local doping effects from the mid-gap states, which could create a potential barrier to hole transport. As a result of this blocked hole transport, EL emission outside of the oxide aperture decreases after aging, as does OBIC signal generation.

Near the oxide aperture edge, the geometry of the VCSEL causes an increase of current density relative to the center of the oxide aperture (current crowding), and a corresponding increase in junction temperature. This may be why the VCSEL failed at the edge of the oxide aperture. This process can be exacerbated by so-called “current shunting” [15], in which current is directed away from the middle of the aperture towards the edges, through hydrogen migration passivating dopant sites. By observing the EL intensity as a function of both time and with spatial resolution, it becomes easier to see that defect formation around the edge of the oxide aperture occurs in sudden, discrete events in small regions, rather than gradually and uniformly.

In order to further understand the nature of the defects which cause the observed OBIC signals and decreases in EL intensity, a FIB was used to prepare both cross-sectional and plan-view TEM samples from several failed VCSELs. Several attempts were made to image these defects, however no crystallographic defects were observed. This is despite having used the same TEM sample preparation and imaging techniques in our facilities to observe crystallographic defects in other VCSEL and high-power edge-emitting laser diode samples [16]. In these previous studies, dislocations were observed, and corresponded spatially with dark-line defects seen in EL and EBIC images. In the current samples, no dark-line defects were observed.

Further measurements are necessary to clarify the microscopic nature of the defects observed, including further TEM imaging, Time-of-Flight Secondary-Ion-Mass-Spectrometry (TOF-SIMS), and Time-Resolved Photoluminescence (TRPL) imaging. The use of TOF-SIMS might allow for the identification of chemical impurities in the sample, which could degrade device performance. The use of TRPL with sub-micron spatial resolution might allow for the evaluation of non-radiative recombination rates, which would aid in the analysis of potential mid-gap state defect concentrations and energies.

## 5. Conclusions

We have presented before/after OBIC images, time resolved EL images, and electrical IV curves from oxide VCSELs measured during accelerated life testing. Both optical measurement techniques identify localized failure sites around the VCSEL oxide aperture, which were temporally correlated with decreased laser power output, and time resolved EL images indicate that these localized failures occur suddenly, rather than gradually over time. Electrical characterization with IV curves also indicates sudden, step-like formation of defects, rather than continuous degradation. The electrically observed failure events are temporally correlated with the optically observed failure

events. The increase in low-injection junction current with a slope corresponding to the *qV/2kT* term in the SRH equation suggests mid-gap trap-state mediated carrier recombination, with a trap state density increasing by ∼250x during device failure. OBIC images also indicate mid-gap defect states localized near the oxide aperture. These mid-gap trap states create non-radiative pathways for carrier re-combination, reducing light output from the VCSEL during operation. A hypothesis was presented attributing the location of the defects around the oxide aperture edge to current crowding in that area, which increases local electrical and thermal stress. The results reported here may be useful for informing failure models for VCSEL devices used in high-reliability applications.

## References


[1] S. B. Healy *et al.*, "Active region design for high-speed 850-nm VCSELs," *IEEE J. Quantum Electron.*, vol. 46, no. 4, pp. 506–512, Apr. 2010.

[2] S. Blokhin *et al.*, "Oxide-confined 850 nm VCSELs operating at bit rates up to 40 Gbit/s," *Electron. Lett.*, vol. 45, no. 10, pp. 501–503, May 2009.

[3] T. Anan *et al.*, "High-speed 1.1-$\mu$m-range InGaAs VCSELs," in *Proc. Opt. Fiber Commun./Nat. Fiber Opt. Engineers Conf.*, 2008, pp. 1–3.

[4] R. H. Johnson and D. M. Kuchta, "30 Gb/s directly modulated 850 nm datacom VCSELs," in *Proc. Conf. Lasers Electro-Optics*, 2008, Paper CPDB2.

[5] D. M. Kuchta *et al.*, "A 56.1 Gb/s NRZ modulated 850 nm VCSEL-based optical link," in *Proc. Opt. Fiber Commun. Conf. Expo. Nat. Fiber Opt. Engineers Conf.*, 2013, pp. 1–3.

[6] C. J. Helms, I. Aeby, W. Luo, R. W. Herrick, and A. Yuen, "Reliability of oxide VCSELs at Emcore," in *Proc. Integr. Optoelectron. Devices*, 2004, pp. 183–189.

[7] R. W. Herrick, "Oxide VCSEL reliability qualification at Agilent Technologies," in *Proc. Symp. Integr. Optoelectron. Devices*, 2002, pp. 130–141.

[8] R. W. Herrick, "Design for reliability and common failure mechanisms in vertical cavity surface emitting lasers," in *Proc. MRS* , 2012, pp. g01–04.

[9] R. W. Herrick, "Reliability and degradation of vertical-cavity surface-emitting lasers," in *Materials and Reliability Handbook for Semiconductor Optical and Electron Devices*, O. Ueda and S. J. Pearton, Eds. New York, NY, USA: Springer, 2013, pp. 147–205.

[10] Y. Sin, N. Ives, N. Presser, and S. C. Moss, "Failure mode investigation of high power multi-mode InGaAs-AlGaAs strained quantum well lasers using time-resolved EL and EBIC techniques," in *Proc. Int. Quantum Electron. Conf.*, 2009, Paper JTuD16.

[11] S. M. Sze and K. K. Ng, *Physics of Semiconductor Devices*. New York, NY, USA: Wiley, 2006.

[12] C. Lei *et al.*, "Emcore VCSEL failure mechanism and resolution," *Proc. SPIE*, vol. 7615, 2010, Art. no. 761504.

[13] R. A. Falk, "Advanced LIVA/TIVA techniques," in *Proc. Int. Symp. Testing Failure Anal.*, 2001, pp. 59–68.

[14] E. Cole Jr., P. Tangyunyong, D. Benson, and D. Barton, "TIVA and SEI developments for enhanced front and backside interconnection failure analysis," *Microelectron. Rel.*, vol. 39, no. 6/7, pp. 991–996, 1999.

[15] T. Abe, H. Fukuda, Y. Iriyama, and Z. Ogumi, "Solvated Li-ion transfer at interface between graphite and electrolyte," *J. Electrochem. Soc.*, vol. 151, no. 8, pp. A1120–A1123, 2004.

[16] Y. Sin, Z. Lingley, N. Presser, M. Brodie, N. Ives, and S. C. Moss, "Catastrophic optical bulk damage in high-power InGaAs-AlGaAs strained quantum well lasers," *IEEE J. Sel. Topics Quantum Electron.*, vol. 23, no. 6, Nov./Dec. 2017, Art. no. 1500813.